Layer configuration-driven phase engineering of Sol-Gel epitaxial $Pb(Zr,Ti)O_3$ thin films for high piezoelectricity on silicon substrate

Kweon, Sang Hyo

Kasatani, Kota

Kanno, Isaku

(Citation)
Acta Materialia,311:122162

(Issue Date)
2026-06-01

(Resource Type)
journal article

(Version)
Version of Record

Acta Materialia 311 (2026) 122162

Contents lists available at ScienceDirect

Acta Materialia

journal homepage: www.elsevier.com/locate/actamat

Full length article

Layer configuration-driven phase engineering of Sol-Gel epitaxial $Pb(Zr,Ti)O_3$ thin films for high piezoelectricity on silicon substrate

Sang Hyo Kweon [1], Kota Kasatani [1], Isaku Kanno [*]

Department of Mechanical Engineering, Kobe University, 1-1 Rokkodai-cho, Nada-ku, Kobe 657-8501, Japan

ARTICLE INFO

Keywords:
PZT thin film
Epitaxial growth
Hetero-layered
Sol-gel
piezoelectric property
Si substrate

ABSTRACT

In this study, we investigate piezoelectric behavior of sol-gel derived epitaxial $Pb(Zr,Ti)O_3$ (PZT) thin films with hetero-layered (HL) configurations on Si substrates. HL*x*/*y* films are fabricated by stacking two PZT layers with the same or different Zr/Ti ratios, where *x* and *y* indicate the Zr contents of the first and second layers, respectively, and this bilayer sequence is repeated throughout the film. We examine HL52/52 (equal to single-composition-deposited film, SCD52), HL60/45, and HL45/60, which share almost identical average compositions, to investigate how the stacking sequence affects film properties. Furthermore, *in-situ* bias-resolved reciprocal space mapping (RSM) is employed to elucidate the electric-field-induced structural responses associated with their piezoelectric behavior. We extend our discussion to films with various layer configurations, where they are classified into four structural types; α-, β-, γ-, and δ-PZT. The effective transverse piezoelectric coefficient, $|e_{31,f}|$, is evaluated under both positive and negative unipolar oscillations. A clear correlation is found between the crystal structure and the built-in electric field (BIEF) direction, which significantly influences $|e_{31,f}|$. Notably, the highest $|e_{31,f}|$ values are found near the morphotropic phase boundary (MPB): HL45/60 achieves 15.9 C m^{-2} under negative unipolar oscillation, while HL60/45 reaches 13.5 C m^{-2} under positive unipolar oscillation. These results demonstrate that by tailoring the layer configuration, the piezoelectric response of sol-gel derived epitaxial PZT thin films can be effectively optimized.

1. Introduction

Since piezoelectric $Pb(Zr,Ti)O_3$ (PZT) thin films serve as key materials for piezoelectric micro-electromechanical systems (piezo-MEMS), their piezoelectric properties have been extensively studied to enhance the performance of these devices [1–4]. In terms of crystallinity, PZT thin films used in piezo-MEMS have been predominantly polycrystalline. In particular, a recent study reported highly textured PZT films with remarkable improvements in the 33-mode piezoelectric charge coefficient (d_{33}) [5]. In addition, polycrystalline and textured PZT thin films have demonstrated effective transverse piezoelectric coefficients ($|e_{31,f}|$) reaching the mid-teens C m^{-2} under optimized crystal structure, preferred orientation, and processing conditions [1,2].

However, the performance of practical piezo-MEMS devices is not determined solely by the piezoelectric coefficient in most cases. Instead, device-level efficiency can depend on additional physical quantities that vary with the specific application. For instance, in piezoelectric energy harvester (PEH), gyroscope, and piezoelectric micromachined ultrasound transducer (pMUT) applications, the figure of merit (FOM) is expressed as $(|e_{31,f}|)^2/(\varepsilon_0\varepsilon_r)$, where ε_0 and ε_r represent the vacuum permittivity and the dielectric constant, respectively, illustrating that a large dielectric constant can suppress device performance even when $|e_{31,f}|$ is high [6–8]. As polycrystalline and textured thin films possess relatively high dielectric constants, their FOMs in the above applications tend to be limited. More generally, such films are likely to be utilized only in piezo-MEMS devices where the FOM is primarily determined by the magnitude of the piezoelectric coefficient. To address this limitation from the perspective of device-level performance, many efforts have been made to deposit epitaxial PZT thin films [9–15]. The films have demonstrated good piezoelectric coefficients along with stable voltage and displacement responses (piezoelectric linearity) [16]. Besides, high Curie temperature (T_c), large electromechanical coupling coefficients, and markedly small dielectric constants that are desirable for enhanced device performance have also been reported [7,8,16].

On top of that, the crystallinity of thin films profoundly influences how clearly the relationship between crystal structure and piezoelectric

* Corresponding author.
E-mail address: kanno@mech.kobe-u.ac.jp (I. Kanno).
[1] S. H. Kweon and K. Kasatani contributed equally to this work.

https://doi.org/10.1016/j.actamat.2026.122162
Received 19 August 2025; Received in revised form 18 March 2026; Accepted 25 March 2026
Available online 26 March 2026

response can be identified. Epitaxial PZT thin films offer a distinct advantage in this regard, because their well-defined crystallinity removes the ambiguity caused by orientation inhomogeneity in polycrystalline films (throughout the entire film) and in textured films (throughout the in-plane direction). This crystallographic clarity enables more definitive identification of how crystal structure governs piezoelectric response, which underscores the importance of epitaxial PZT thin films for piezo-MEMS, even with recent advances in textured-film techniques.

Typically, oxide single-crystal substrates such as $SrTiO_3$ and MgO have been used for epitaxial growth due to their small lattice mismatches of <5% [9–12]. However, since compatibility with conventional MEMS microfabrication processes is essential, the deposition of epitaxial PZT thin films on Si substrates is highly desired. Accordingly, several studies have focused on demonstrating the successful deposition of epitaxial PZT thin films on Si substrates [13–19]. Among these approaches, sputtering has been the most widely employed method for depositing epitaxial PZT thin films on Si substrates, as it enables the production of high-quality films with excellent piezoelectric properties through precise control over composition [16–23]. This advantage was particularly evident in our previous work, where a maximum $|e_{31,f}|$ of 10.1 C m^{-2} was achieved in a rhombohedral-dominant morphotropic phase boundary (MPB) under the direct piezoelectric effect, whereas a tetragonal-dominant MPB exhibited a maximum $|e_{31,f}|$ of 14.0 C m^{-2} under the converse piezoelectric effect [16].

Recently, the sol-gel method has gained attention as a promising candidate for depositing epitaxial PZT thin films in piezo-MEMS applications [24–29]. A maximum converse $|e_{31,f}|$ of 12.5 C m^{-2} which is comparable to that of sputtered epitaxial PZT thin films, was obtained from sol-gel derived films at the MPB [28]. This enhancement was attributed to electric-field-induced strain and 90° domain wall motion under an applied voltage, which was observed using bias-resolved *in-situ* analysis via synchrotron radiation X-ray diffraction (SR-XRD).

To enhance the piezoelectric properties further, a new approach is required to facilitate electric-field-induced strain and domain wall motion in response to an applied voltage. It was shown that constructing a hetero-layered (HL) PZT which consists of PZT layers with different Zr/Ti ratios, is an effective way to improve the piezoelectric, ferroelectric and dielectric properties of sol-gel derived PZT thin films by enabling film texture control [30], phase boundary engineering [31], field-induced coupling [32–33], and strain gradient formation [5,34]. Since previously reported HL PZT thin films were typically polycrystalline, applying the HL concept to epitaxial films enables a crystallographically well-defined investigation of how layer configuration, defined as the specific combination of composition and stacking sequence, affects their properties.

In this study, we prepared *c*-axis oriented epitaxial PZT thin films on (001)$SrRuO_3$ (SRO)/Pt/ZrO_2/Si substrate using the sol-gel method. To unravel the relationship between layer configuration and piezoelectric properties, we first examined a set of films designed to have nearly identical average compositions but different layer configurations. In this comparative study, the epitaxial nature enabled us to systematically investigate the correlation among crystal structures (as revealed by reciprocal lattice mapping, RSM), built-in electric fields (BIEF), and piezoelectric properties. To further clarify the electric-field-induced structural responses, we also employed bias-resolved *in-situ* SR-XRD. Building upon these insights, our study expanded to explore a wider spectrum of PZT layer configurations and correlated the piezoelectric responses with their crystal structures and BIEF. Through this comprehensive approach, we aimed to generalize design parameters for effectively optimizing the piezoelectric performance of HL PZT thin films, in particular, on Si substrate for piezo-MEMS applications.

2. Experimental methods

Preparation of sol-gel derived epitaxial PZT thin films: Epitaxial PZT thin films with thicknesses of 1.0–1.4 μm were deposited on (001)SRO/Pt/ZrO_2/Si (KRYSTAL) using the sol-gel method. In this substrate structure, the SRO and Pt bottom stack is epitaxially grown on the underlying ZrO_2 buffer layer, which enables the epitaxial growth of the PZT films. Five types of precursor solutions were employed, namely, PZT30, PZT45, PZT52, PZT60, and PZT70, where the numbers represent the Zr fraction at the B-site (e.g., PZT52 corresponds to Zr/Ti = 52/48). Excess Pb was added to compensate for Pb evaporation during annealing. The solution concentration was adjusted to 15 wt%. The deposition process was as follows; the precursor solution was spin-coated onto the Si substrate, followed by pre-baking at 300 °C on a hot plate. This sequence was repeated to deposit two layers, forming one bilayer. Crystallization of each bilayer was carried out via rapid thermal annealing (RTA, Advance RIKO, MILA-5000) at 650 °C for 3 min. By controlling the composition and stacking sequence, PZT thin films with differed layer configurations were fabricated. A total of 12 PZT layers were deposited through six repetitions of the above process. The films are described according to the Zr contents of the first and second layers. For instance, HL45/60 refers to a film with the first layer of PZT45 and the second layer of PZT60. Among the HL PZT, in cases where the first and second layers had the same compositions, that is, films grown from a single PZT composition, they are hereafter referred to as single-composition-deposited (SCD) PZT thin films (e.g., HL52/52 is identical to SCD52). From the prepared films, three films with nearly identical average compositions (SCD52, HL60/45, and HL45/60) were selected for the initial comparison, and their layer configurations are illustrated schematically in Fig. 1. This schematic provides a structural reference for the subsequent analyses.

Compositional, crystal structure, and microstructural characterization: Compositional depth profiles of the PZT thin films were analyzed using X-ray photoelectron spectroscopy (XPS, ULVAC-PHI, Quantera-SXM). Crystal structures were evaluated by XRD (RIGAKU, MultiFlex) with CuKα radiation (λ = 1.54 Å). Out-of-plane measurements were carried out in $\theta/2\theta$ mode, in-plane φ-scan measurements were conducted, and RSM images were obtained around the $PZT(204)_{pc}$ (where pc denotes the pseudocubic coordinate) reciprocal lattice node. For more precise analysis, SR-XRD was conducted at SPring-8, beamline BL46XU, using monochromatic X-rays (12.4 keV, λ = 1.0 Å). Bias-resolved *in-situ* 2θ-χ diffraction images were obtained under DC biases ranging from −20 to 0 V. These images were taken around the $PZT(103)_{pc}$ and $PZT(004)_{pc}$ reciprocal lattice nodes and were captured using a two-dimensional X-ray photon-counting pixel detector (DECTRIS, PILATUS3 × 300 K), while changing the incident angle ω. The resulting images were then converted to RSM images in Q_z-Q_x coordinates. For microstructural observation, scanning electron microscope (SEM, HITACHI, S-4100) was employed. Piezoresponse force microscopy (PFM) measurements were performed to probe the local electromechanical response at the film surface using an atomic force microscope (AFM, BRUKER, Dimension Icon) equipped with a lock-in amplifier. Both vertical and lateral PFM signals were collected.

Evaluation of dielectric, ferroelectric, and piezoelectric properties: To measure electric properties, dot-shaped Pt top electrodes with a diameter of 300 μm were deposited to form a metal-insulator-metal (MIM) structure. Dielectric properties were measured using an LCR meter (NF, ZM2372), and ferroelectric hysteresis curves were recorded using a ferroelectric tester (RADIANT, Multiferroic II) at 1 kHz. The converse piezoelectric properties were evaluated using the unimorph cantilever method, as described in our several past studies [22,35]. A schematic illustration is provided in **Figure S1** (Supplementary material). Cantilevers were cut to dimensions of approximately 20 mm x 2 mm. Prior to the operation of cantilevers, poling process was implemented by applying either a positive or negative unipolar oscillation (1 kHz, 20 V_{pp}) for 1 min using a function generator (NF, WF1943B) with an add-on power amplifier (NF, 4015), indicating that the poling was carried out through direct electrical contact. For the measurement of converse $|e_{31,f}|$, both positive and negative unipolar oscillations ranging from 5 to 20 V_{pp} were applied to the clamped cantilever using a function generator

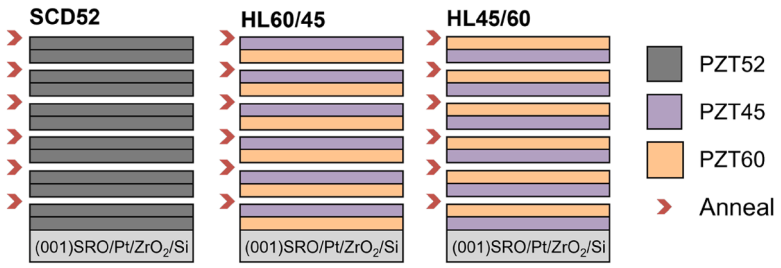

Fig. 1. Schematic illustrations of sol-gel derived epitaxial PZT thin films: SCD52, HL60/45, and HL45/60. A total of 12 PZT layers were sequentially deposited along the thickness direction, with crystallization conducted by annealing after every two layers (i.e., each bilayer).

(NF, WF1946A), and the resulting tip displacement was detected by a laser Doppler vibrometer (GRAPHTEC, AT1100).

3. Results and discussion

3.1. Impact of layer configuration on composition and crystallography in HL PZT thin films

Compositional depth profiles of SCD52, HL60/45, and HL45/60, obtained using XPS, are plotted in Fig. 2. The deposition history of every bilayers, along with the interfaces between bilayers where annealing for crystallization was implemented, is also illustrated. Although the Pb composition remained almost constant, fluctuations in the B-site elements, Zr and Ti, were evident in all films along the thickness direction. In addition, bilayers deposited at earlier stages exhibited relatively blurred compositional changes at the interfaces, because of the diffusion of Zr and Ti elements during continuous annealing. For the compositional variations of other elements, refer to **Figure S2**.

In SCD52, Zr and Ti compositional gradients were observed within each bilayer, despite this film being nominally a single-composition stack. Specifically, a Ti-rich composition dominated the bottom of each bilayer, whereas a Zr-rich composition existed at the upper side. This phenomenon can be attributed to the crystallization of the Ti-rich composition, which is energetically favorable in the presence of heterogeneous nucleation sites such as the substrate or a preceding bilayer [31,36]. At these sites, Ti-rich PZT nucleates at a relatively lower temperature or with a higher nucleation rate than Zr-rich PZT, resulting in the formation of compositional gradients within each bilayer. In contrast, in HL60/45, where the first layer was Zr-rich PZT60, the insufficient diffusion time for Ti elements from the PZT45 layer to reach the nucleation sites during crystallization resulted in a relatively homogenized Zr and Ti compositional profile (gradient-free) compared to SCD52. Meanwhile, HL45/60 with PZT45 as the first layer, exhibited intensified Zr and Ti compositional gradients, manifesting a trend similar to that of SCD52. These results demonstrate that compositional distributions in sol-gel derived PZT thin films can be effectively tuned through PZT layer configuration control, and concurrently provide valuable insights into the underlying mechanisms of phase evolution.

The crystallographic characteristics of the sol-gel derived PZT thin films are depicted in Fig. 3, which presents RSM images around the PZT $(204)_{pc}$ reciprocal lattice node. To complement the RSM, the out-of-plane XRD patterns were taken (**Figure S3(a)**), verifying that the films were preferentially oriented along the $[001]_{pc}$ direction. The overlapping (002) diffraction peaks suggest the coexistence of multiple phases or domain structures within the films. The in-plane φ-scan results (**Figure S3(b)**) showed clear four-fold symmetry, indicating well-defined in-plane crystallographic alignment of the films. Based on these observations, the RSM images in Fig. 3 provide a more detailed visualization of the crystal structures, confirming the epitaxial growth of the PZT thin films on Si substrates.

In our previous study, the diffraction patterns of SCD52 were identified as originating from tetragonal (*T*) phase with *a*- and *c*-domains [28], hereafter referred to as *a*-*T* and *c*-*T*, respectively. However, the XPS

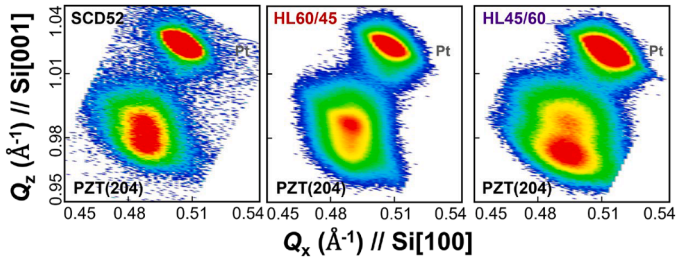

Fig. 3. RSM images obtained from SCD52, HL60/45, and HL45/60 around the $PZT(204)_{pc}$ reciprocal lattice node.

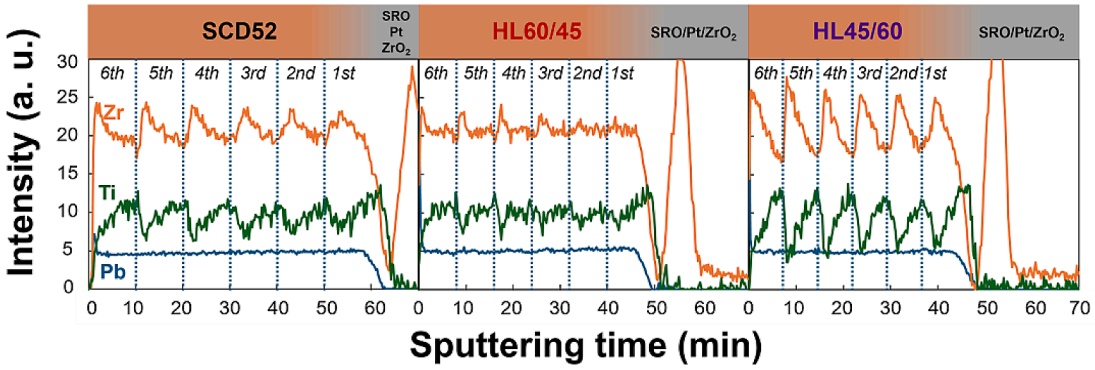

Fig. 2. Compositional depth profiles of SCD52, HL60/45, and HL45/60 obtained by XPS for Pb, Zr, and Ti. The deposition history and timing of crystallization for each bilayer are presented, as well. A sudden rise in Zr at the substrate corresponds to the ZrO_2 seed layer used to promote the epitaxial growth of the (001)Pt bottom electrode. Full elemental profiles including O and Pt are available in **Figure S2**. The depth is represented by the sputtering time (min), which reflects the relative depth from the film surface.

results in Fig. 2 clearly revealed the coexistence of Ti-rich and Zr-rich compositions within each bilayer, which cannot be fully explained by the presence of the *T* phase alone. Besides, as will be discussed later, a progressive transformation from the *a*-*T* to the rhombohedral (*R*) phase was confirmed as the Zr content in the second layer increased. Hence, it is reasonable to assign the two distinct diffraction spots observed in SCD52 to the Ti-rich *c*-*T* (bottom, with lattice constants of $a = 4.096$ Å and $c = 4.102$ Å), and to a combined contribution from *a*-*T* and Zr-rich *R* phase (upper, where the lattice constants are difficult to define), respectively. It is also worth mentioning that the *T* phase containing *a*-*T* and *c*-*T* in this study is associated with a mosaic microstructure, which manifests as a faintly elongated diffraction feature in RSM images [28]. Moreover, the vertically aligned diffraction spots found in SCD52 suggest that the in-plane lattice constants for all phases were nearly the same. Considering that the in-plane lattice constant of the *c*-*T* is inherently smaller than those of the *a*-*T* and *R* under stress-free conditions, this phenomenon is likely attributed to internal stress exerted along the in-plane directions: tensile stress on the *c*-*T* and compressive stress on the *a*-*T* and *R*. It is regarded that the alternately stacked phases imposed mutual strain along the in-plane direction, thereby giving rise to the vertically aligned features in the RSM image.

As discussed in Fig. 2, HL60/45 exhibited a gradient-free compositional profile along the thickness direction, indicating a nearly homogeneous composition close to PZT52. This led to the formation of an almost purely *R* phase structure with $a = 4.076$ Å, as confirmed by the RSM image. A minor presence of mosaic *T* phase was also identified, as evidenced by a slightly elongated diffraction feature. However, the development of the *T* phase appeared too weak to be regarded as a distinct phase; rather, it is considered to reflect a locally formed lattice gradient within the dominant *R* phase. In this context, it can be inferred that the internal stress arising from lattice mismatch between coexisting phases, which was pronounced in SCD52, was effectively minimized in this film.

Regarding HL45/60, the presence of compositional gradients in Zr and Ti suggests that phase separation occurred via a mechanism similar to that of SCD52. Nevertheless, due to the altered layer configuration, the evolved crystal structure was a bit different from that of SCD52. Two distinct, vertically aligned diffraction spots were observed in the RSM image, corresponding to the Ti-rich *c*-*T* (bottom, with lattice constants of $a = 4.088$ Å and $c = 4.110$ Å) and the Zr-rich *R* phase (upper, $a = 4.076$ Å). This argument could be backed up with the emergence of the *R* phase, arising from the transformation of *a*-*T* as the Zr content in the second layer increased, as previously discussed. Moreover, the diffraction pattern associated with the mosaic structure was not found in HL45/60, indicating that the upper spot corresponds solely to the *R* phase. Meanwhile, the tetragonality of the bottom spot became more pronounced, as reflected in the decrease of the *a*-axis and increase of the *c*-axis compared to SCD52, which can be attributed to the enhanced Ti concentration at the bottom of each bilayer.

As a complementary observation, SEM images are provided in **Figure S4** to examine the microstructural features of SCD52, HL60/45, and HL45/60. Any traces of mosaic structure and lattice gradient found in the RSM data were not resolved within the spatial resolution of SEM. The absence of secondary phases in the surface images confirmed the structural stability of the epitaxial thin films during crystallization. In addition, PFM measurements were conducted for these films, and the results are provided in **Figure S5**.

Overall, the XPS compositional distributions and RSM crystallographic analyses revealed that the layer configuration directly influences the resulting compositional gradients, which in turn govern the phase evolution during the crystallization process. This understanding is essential for engineering desired crystal structures, and its significance for functional properties will be discussed in subsequent sections.

3.2. Ferroelectric and piezoelectric properties under the influence of BIEF

Fig. 4 presents the polarization-electric field (*P*-*E*) hysteresis curves of the sol-gel derived epitaxial PZT thin films. These films exhibited clear ferroelectric switching behavior, without any notable differences among the three PZT film types. A slanted hysteresis shape was obtained from these films, which stemmed from a substantial paraelectric contribution to total polarization. This interpretation is supported by the exceptionally large dielectric constants, regardless of their compositional distribution or crystal structure. Although the exact origin of the large dielectric constants has not been fully addressed yet, the discontinuous growth mechanism inherent to sol-gel deposition is believed to play a key role. This growth behavior induced domain boundary formation not only within each bilayer, as discussed in the previous section, but also at the interfaces between bilayers. According to previous microscopic observations, ferroelectric polarization tends to be greatly disordered at domain boundaries [37], making it reasonable to conclude that the large dielectric constants in the thickness direction were unavoidable in this study. Furthermore, a gradual polarization reversal was observed, due to the difficulty in domain-wall movements across bilayer interfaces.

Meanwhile, the hysteresis curves for SCD52 and HL60/45 manifested an imprint toward the negative direction, suggesting the presence of a BIEF within the thin films. In contrast, a nearly centered hysteresis was observed for HL45/60. These results indicate that the stable polarization direction was downward (upward BIEF) for SCD52 and HL60/45, and upward (downward BIEF) for HL45/60, which will be revisited in the following discussion.

To investigate the 31-mode piezoelectric responses of the PZT thin films, the converse $|e_{31,f}|$ was evaluated using the cantilever method under unipolar voltage oscillation, as shown in Fig. 5. In this study, both positive and negative unipolar oscillations were applied, since asymmetrical behavior in the converse $|e_{31,f}|$ is generally observed in epitaxial PZT thin films. For clarity, the converse $|e_{31,f}|$ measured under positive and negative unipolar oscillations are hereafter denoted as $|e_{31,f}|^+$ and $|e_{31,f}|^-$, respectively, while $\Delta|e_{31,f}|^+$ and $\Delta|e_{31,f}|^-$ represent their respective variations across the 5–20 V_{pp} range. Under a positive

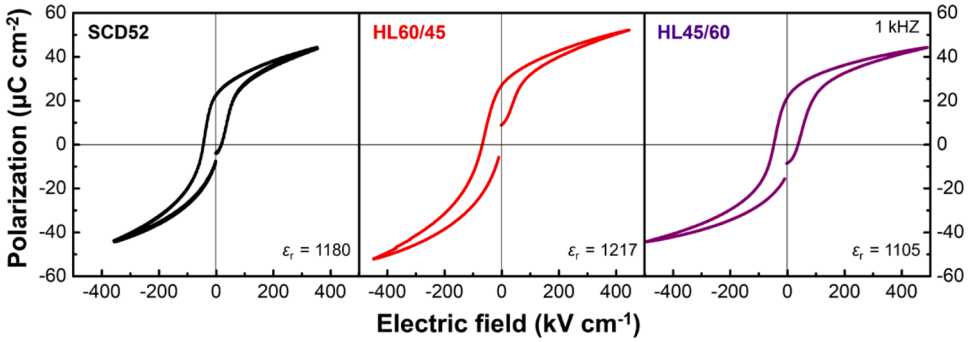

Fig. 4. *P*-*E* hysteresis curves and dielectric constants measured for SCD52, HL60/45, and HL45/60 at 1 kHz.

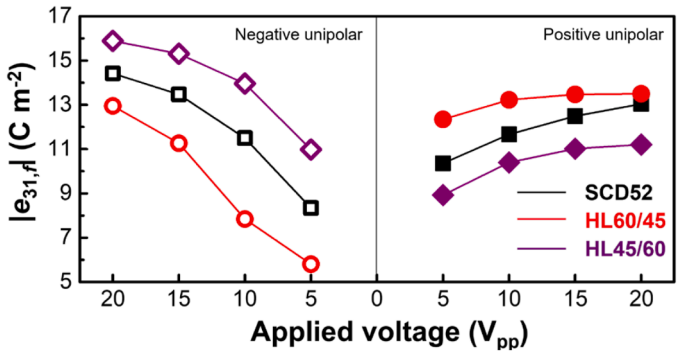

Fig. 5. Converse $|e_{31,f}|$ observed from SCD52, HL60/45, and HL45/60 under both positive and negative unipolar oscillations in the 5–20 V_{pp} range. Asymmetric behaviors between $|e_{31,f}|^+$ and $|e_{31,f}|^-$ are clearly shown.

unipolar oscillation, HL60/45 exhibited the highest $|e_{31,f}|^+$ value of 13.5 C m^{-2} at 20 V_{pp}, with a small $\Delta|e_{31,f}|^+$ of 1.2 C m^{-2}. In contrast, HL45/60 recorded the lowest $|e_{31,f}|^+$ value of 11.2 C m^{-2}. Conversely, when a negative unipolar oscillation of 20 V_{pp} was applied, HL45/60 showed the highest $|e_{31,f}|^-$ of 15.9 C m^{-2}, with a $\Delta|e_{31,f}|^-$ of 4.9 C m^{-2}, while HL60/45 exhibited the lowest value of 12.9 C m^{-2}. Specifically, both the $|e_{31,f}|^-$ of 15.9 C m^{-2} for HL45/60 and $|e_{31,f}|^+$ of 13.5 C m^{-2} for HL60/45 represent noteworthy advancements compared to our previous reports on both sputtered (14.0 C m^{-2}) and sol-gel epitaxial PZT thin films (12.5 C m^{-2}) [16,28]. This is particularly significant considering the cost-effective and silicon-compatible sol-gel process, demonstrating our capability to achieve high performance while maintaining fabrication simplicity. Meanwhile, the asymmetric behaviors were further supported by tip displacement measurements as a function of applied voltage (**Figure S6**). In both SCD52 and HL60/45, the voltages corresponding to the minimum displacements were asymmetric with respect to 0 V, with the negative voltage having a greater magnitude than the positive one, indicating the presence of an upward BIEF. On the other hand, HL45/60 exhibited nearly symmetric displacement minima, with comparable voltage magnitudes on both the positive and negative sides, implying a negligible BIEF. These results are well consistent with those from the *P-E* hysteresis curves in Fig. 4, where BIEFs were confirmed through 33-mode measurements.

Considering that HL60/45 was found to predominantly have an *R* phase based on the present XRD results, it is natural to say that this phase stabilized the upward BIEF. Such an upward BIEF could support effective dipole alignment and reinforce the piezoelectric response even at relatively low applied voltages. As a result, HL60/45 achieved the highest $|e_{31,f}|^+$ value. By the same reason, its small $\Delta|e_{31,f}|^+$ can be explained. On the contrary, the presence of the upward BIEF probably suppressed the response under negative unipolar oscillation, leading to reduced $|e_{31,f}|^-$ and a relatively large $\Delta|e_{31,f}|^-$.

In contrast, HL45/60 exhibited a negligible BIEF, indicating that the dipole moments originating from the minor *R* phase may have been cancelled by the dominant *c-T* phase. In this context, the *c-T* phase is presumed to induce a downward BIEF, and its proportion in the thin film is thought to serve as a barometer for the $|e_{31,f}|^-$. Accordingly, HL45/60 showed the highest $|e_{31,f}|^-$ among the three kinds of films. However, $\Delta|e_{31,f}|^-$ remained relatively large owing to the absence of a strong BIEF, unlike HL60/45 where the stable upward BIEF enabled a small $\Delta|e_{31,f}|^+$.

SCD52 showed a phase fraction intermediate between HL45/60 and HL60/45, containing less *c-T* which is directly related to downward BIEF, than HL45/60 but more than HL60/45. As a result, its piezoelectric properties also fell between those of the two films, consistent with its moderate proportions of the *a-T, c-T*, and *R* phases.

3.3. *In-situ* structural analysis of intrinsic and extrinsic contribution to $|e_{31,f}|^-$

To investigate the structural mechanisms underlying the converse piezoelectric response in HL45/60, *in-situ* RSM images were acquired under applied DC bias ranging from −20 to 0 V using SR-XRD. This technique is a powerful tool for precisely and directly dissecting the interplay of intrinsic and extrinsic contributions for piezoelectricity in real-time [28], being enabled by our high-quality epitaxial films. In this study, to minimize overlapping of diffraction spots from multiple phases, the reciprocal lattice node around PZT(004)$_{pc}$ was selected, and visualized in Fig. 6**(a)**. The lattice strain of the *c-T* and *R* phase along the [001]$_{pc}$ direction ($\Delta L_{c\text{-}T}$ and ΔL_R, respectively) was quantified relative to their lattice constants at 0 V. Besides, the fractional intensities, defined as $I_{c\text{-}T}/(I_{c\text{-}T} + I_R)$ and $I_R/(I_{c\text{-}T} + I_R)$, where $I_{c\text{-}T}$ and I_R correspond to the diffraction intensities of the *c-T* and *R*, respectively, were calculated and plotted in Fig. 6**(b)**. Note that the DC bias sequence was started from −20 V to ensure that the dipole moments were aligned in the upward direction. Otherwise, dipoles that had been rotated to other directions in preceding measurements could cause underestimation at low DC bias levels.

As the applied DC bias increased from −20 to 0 V, the RSM coordinates of diffraction spots for both *c-T* and *R* phase gradually shifted, indicating changes in the *c*-axis lattice constants. The maximum lattice strain appeared at −20 V, where the *c*-axis lattice strains of the *c-T* and *R* reached 0.23% and 0.14%, respectively. These lattice expansions are attributed to intrinsic contributions to the converse piezoelectric response. Simultaneously, noticeable changes in diffraction intensities were also detected. The fractional intensity of the *R* phase decreased from 0.29 to 0.27, while that of the *c-T* increased from 0.71 to 0.73. This change in diffraction intensity suggests an electric-field-induced phase transformation from the *R* phase to the *c-T*. Because this phase transformation involves the motion of phase boundaries and structural reconfiguration, it is regarded as an extrinsic contribution to the converse piezoelectric response.

In our previous *in-situ* RSM study, SCD52 was shown to have cooperative activation of intrinsic (lattice strain of *c-T*) and extrinsic (*a-T* to *c-T* domain switching) contributions under applied bias. This contrasted with PZT thin films that were predominantly governed by a single-type contribution (SCD45 by extrinsic *a-T* to *c-T* domain switching, and SCD60 by intrinsic *R* lattice strain) [28]. Owing to this cooperative activation, SCD52 was believed to exhibit better piezoelectric properties compared to SCD45 and SCD60. HL45/60 in this work, as mentioned above, also displayed the cooperative activation of both intrinsic (lattice strain of *c-T* and *R*) and extrinsic (*R* to *c-T* phase transformation) contributions, which was instrumental in achieving the $|e_{31,f}|^-$ of 15.9 C m^{-2}. Meanwhile, unlike SCD52 in which only the *c-T* among three coexisting phases (*a-T, c-T*, and *R*) was involved, the lattice strain of all existing phases (*c-T* and *R*) was clearly observed in HL45/60, leading to relatively large piezoelectricity. It is considered that the relieved mosaic structure in HL45/60 facilitated this lattice strain response, which is evidenced by the absence of lattice strain in mosaic-structured SCD45 [28]. Based on these results, it is inferred that the participation of all phase components in lattice strain, responding more effectively to the applied bias, contributed to the superior piezoelectric performance in HL45/60.

3.4. *Influence of layer configuration on phase evolution and piezoelectric behavior of HL PZT thin films*

The findings discussed above clearly show that variations in crystal structure, driven by modified compositional gradients, played a critical role in determining the piezoelectric responses of HL PZT thin films, depending on the direction of the applied unipolar oscillation. To gain a more comprehensive understanding of this behavior, we further investigated a wide range of PZT layer configurations. The ranges of $|e_{31,f}|$

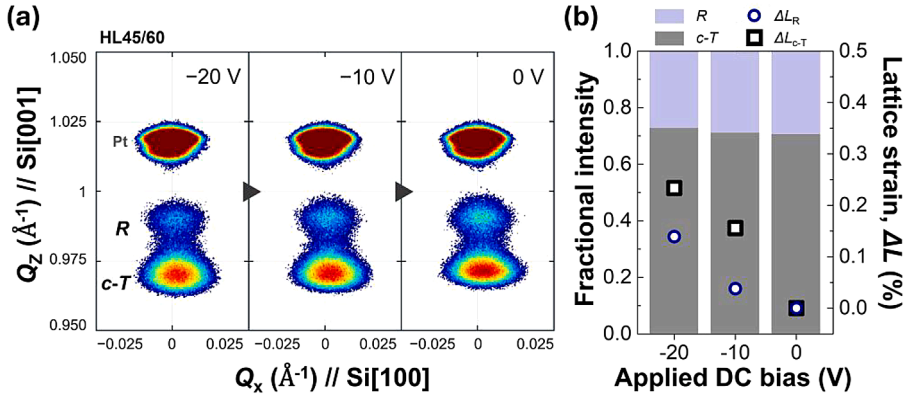

Fig. 6. (a) Bias-resolved *in-situ* RSM images acquired from HL45/60 around the PZT(004)$_{pc}$ reciprocal lattice node under applied DC bias. (b) Fractional intensity and lattice strain of the *c-T* and *R*, calculated from the RSM images in (a). The lattice strain were quantified relative to their lattice constants at 0 V. These data offer an insight into the intrinsic and extrinsic contributions to the converse piezoelectric effect.

values under both positive and negative unipolar oscillations are summarized in **Figure S7**, illustrating how the layer configuration influences piezoelectric performance.

Fig. 7 provides RSM images of PZT thin films investigated in this study. These images help clarify how differences in layer configuration give rise to distinct crystal structures. Based on the RSM results, the HL PZT thin films were classified into four crystal structural categories, depending on the compositions of the first and second layers: (i) *α*-PZT, a *T* structure containing both *a*- and *c*-domains, with *a-T* being dominant and featuring a mosaic microstructure. This type appeared when both layers were Ti-rich; (ii) *β*-PZT, a mixed-phase structure composed of *c-T* and *R*, with *c-T* being dominant, observed when the first layer was Ti-rich and the second Zr-rich; (iii) *γ*-PZT, mostly *R* accompanied by a locally formed lattice gradient, found when the first layer was Zr-rich and the second layer Ti-rich; and (iv) *δ*-PZT, a mixture of *R* and pseudocubic (*PC*) phases, occurring when both layers were Zr-rich. In sol-gel derived PZT thin films, such mixed-phase structures are quite natural, because of the inherent difficulty of achieving perfect miscibility along film thickness. Also, it deserves to mention that the thin films located near the boundaries between structural categories often showed intermediate features that reflect characteristics from both adjacent regions.

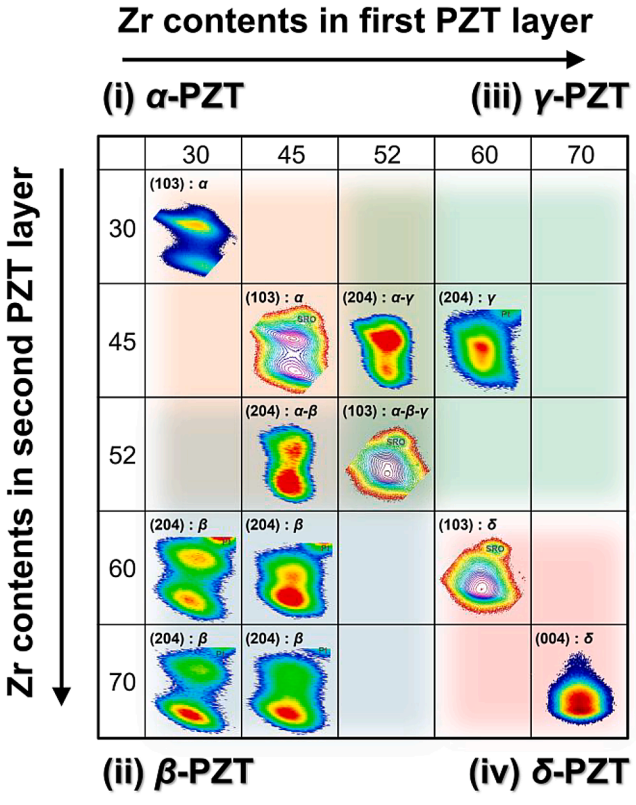

Fig. 7. RSM images collected for a wide range of HL PZT thin films, showing structural evolution with respect to the PZT layer configuration. Four crystal structural categories were defined depending on the compositions of the first and second layers. Here, diffraction patterns around the PZT(103)$_{pc}$ and PZT (004)$_{pc}$ reciprocal lattice nodes were obtained using SR-XRD (λ = 1.0 Å). RSM images for SCD45, SCD52, and SCD60 were taken from our previous work [28].

Besides, *P-E* hysteresis curves are exhibited in **Figure S8**, from which the direction of BIEF in each film can be inferred. In **Figure S7**, the BIEF direction is denoted by plus and minus signs, indicating upward and downward direction, respectively, while a nearly neutral BIEF is represented by a 0. Based on the results, the piezoelectric responses of the HL PZT thin films are elucidated as follows according to their layer configurations.

Regarding the HL30/*x* series (x = 30, 60, and 70), a clear transition in the constituent crystal structure was observed. Initially, HL30/30, which is identical to SCD30, exhibited a diffraction pattern characteristic of the *α*-PZT, as discussed in our previous study [28]. However, when the second layer composition became Zr-rich (as in HL30/60 and HL30/70), the structure evolved into *β*-PZT. This transition was accompanied by the emergence of a downward BIEF, likely due to increased contribution of the *c-T* to the piezoelectric response. As a result, the value of $|e_{31,f}|^-$ increased, while $|e_{31,f}|^+$ decreased. Moreover, the $\Delta|e_{31,f}|^+$ values in the HL30/*x* series were comparable to or even exceeded those of $\Delta|e_{31,f}|^-$, and were significantly larger than those found in other series.

The HL45/*x* series (x = 45, 52, 60, and 70) followed a similar transition mechanism. HL45/45 (SCD45) was governed by the *α*-PZT, which diminished in HL45/52 as it became a *β*-PZT-like intermediate. Due to the strong influence of the *α*-PZT, still the upward BIEF was maintained in these films, causing small $\Delta|e_{31,f}|^+$ and large $\Delta|e_{31,f}|^-$ values. When the Zr content in the second layer reached 60 (HL45/60), despite the crystal structure being nearly *β*-PZT, the BIEF tended toward neutrality, as discussed earlier. Beyond this point, the influence of *α*-PZT vanished, giving rise to a macroscopic downward BIEF. This led to relatively smaller $\Delta|e_{31,f}|^-$ compared to SCD45 and HL45/52.

The HL52/*x* series (x = 45 and 52) also experienced the transition from *α*-PZT to *β*-PZT, under the growing influence of *γ*-PZT, as the Zr content in the second layer increased. The RSM image of HL52/45 reflected an intermediate between *α*- and *γ*-PZT, and HL52/52 (SCD52) exhibited an intermediate among the *α*-, *β*-, and *γ*-PZT crystal structure categories. In the HL60/*x* series (x = 45 and 60), the Zr-rich first layer promoted the formation of *γ*-PZT. As previously described, the

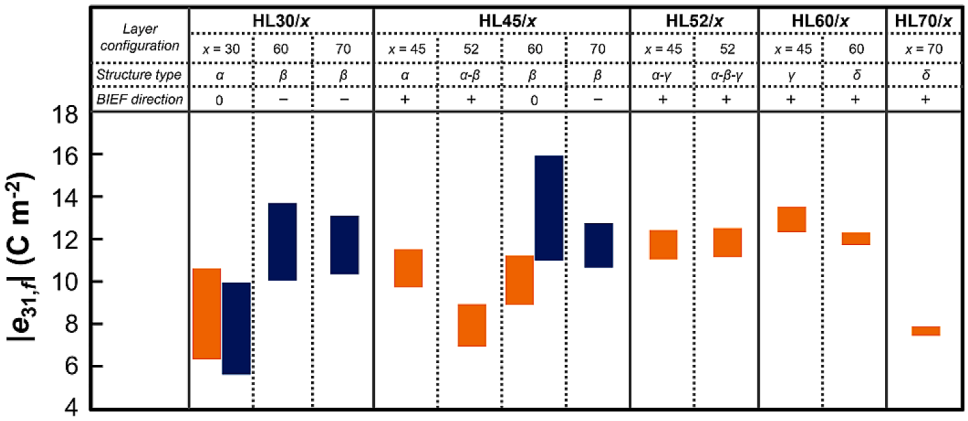

Fig. 8. Comprehensive summary of converse $|e_{31,f}|$ values plotted against the PZT layer configuration. Structure type and BIEF direction are included, as well. Only the $|e_{31,f}|$ aligned with the BIEF direction is shown, while both $|e_{31,f}|^+$ and $|e_{31,f}|^-$ are given for films with neutral BIEF (e.g., SCD30 and HL45/60). Orange and blue bars denote $|e_{31,f}|^+$ and $|e_{31,f}|^-$, respectively.

compositional gradient was not present in HL60/45, resulting in a single *R* phase with lattice gradient. HL60/60 (SCD60) and HL70/*x* ($x = 70$, SCD70) were categorized as *δ*-PZT, in which the *PC* was considered to have negligible influence on the piezoelectric response [28]. In the case of HL52/*x*, HL60/*x*, and HL70/*x*, the *R* phase played an important role in stabilizing dipole alignment, and enabled the construction of an upward BIEF. This stabilization led to large $|e_{31,f}|^+$ values, with the $\Delta|e_{31,f}|^+$ much smaller than $\Delta|e_{31,f}|^-$. However, the maximum $|e_{31,f}|^-$ in some films were found to be comparable to or even larger than the maximum $|e_{31,f}|^+$. Although the exact mechanism has not been figured out yet, this behavior may be related to the relatively homogeneous compositional distribution in these films.

To provide a clear comparison, Fig. 8 summarizes the converse $|e_{31,f}|$ values obtained from the sol-gel derived epitaxial PZT thin films, along with the phase types determined by RSM and the direction of BIEF. For each film, only the $|e_{31,f}|$ value aligned with the BIEF direction is plotted. In cases where the BIEF was nearly neutral, both $|e_{31,f}|^+$ and $|e_{31,f}|^-$ are presented.

When a compositional gradient promoted the development of mainly Ti-rich *c*-*T* along with Zr-rich *R* resulting in the formation of *β*-PZT, a downward or neutral BIEF appeared. A similar downward tendency was also reported for sol-gel derived textured PZT films, where the separation of Ti-rich and Zr-rich regions formed under a compositional gradient was associated with stabilized downward internal fields [5], although the detailed phase identification was not resolved. The downward BIEF led to $|e_{31,f}|^-$ values exceeding $|e_{31,f}|^+$ in this study. Notably, HL45/60 exhibited the highest $|e_{31,f}|^-$ of 15.9 C m^{-2} at 20 V_{pp}, where both intrinsic lattice strain and extrinsic phase transformation contributed cooperatively. This remarkable response can be attributed not only to the cooperative mechanism but also to its favorable phase balance near the MPB. Interestingly, HL30/70 also shares an average composition close to the MPB. However, it displayed a relatively low $|e_{31,f}|^-$ compared to HL45/60. This contrast is perhaps due to intensified phase separation in HL30/70, which disrupted the phase synergy typically expected near the MPB. This phenomenon emphasizes that, while the MPB proximity is undoubtedly important, sophisticated phase tuning is equally critical for maximizing piezoelectric response.

Meanwhile, when *β*-PZT was not the dominant phase, a macroscopic upward BIEF was stabilized. Note that the present dataset did not clarify the microscopic origin of this upward BIEF, and it was therefore described in this study simply as an experimentally observed upward field. Among the films in this group, the HL52/*x* and HL60/*x* series, characterized by *R*-dominant phases and relatively small compositional gradients, exhibited high $|e_{31,f}|^+$values. Especially, HL60/45 had the highest value of 13.5 C m^{-2} at 20 V_{pp}. Its nearly gradient-free compositional profile suppressed phase separation throughout the thickness direction, leading to an almost homogeneous *R*-phase structure that contributed to the strong piezoelectric response. The proximity to the MPB also played an important role, as discussed in the case of negative unipolar oscillation. This observation is in good agreement with a previous report on sol-gel derived polycrystalline PZT films, which emphasized that minimizing compositional gradients improved piezoelectric properties [38].

4. Conclusion

Despite their nearly identical average compositions, the comparative study on SCD52, HL60/45, and HL45/60 revealed substantial differences in piezoelectric performance. HL60/45 exhibited the highest $|e_{31,f}|^+$ value of 13.5 C m^{-2} under positive unipolar oscillation, whereas HL45/60 showed the highest $|e_{31,f}|^-$ value of 15.9 C m^{-2} under negative unipolar oscillation. Meanwhile, SCD52 yielded intermediate responses in both directions. These results clearly suggest that even when the average composition is fixed, the layer configuration critically makes an impact on piezoelectric behavior.

Importantly, our *in-situ* bias-resolved RSM study elucidated the structural mechanism responsible for the enhanced piezoelectricity in HL45/60, which arises from the cooperative activation of both intrinsic (lattice strain of *c*-*T* and *R*) and extrinsic (*R* to *c*-*T* phase transformation) contributions. Notably, all existing phase components (*c*-*T* and *R*) in HL45/60 actively contributed to lattice strain response, unlike SCD52 where only the *c*-*T* among its three coexisting phases (*a*-*T*, *c*-*T*, and *R*) was active [28]. This comprehensive participation of all phases is inferred to be a key factor in enhancing the piezoelectric performance in HL45/60.

Further investigation into a broader range of HL PZT thin films offered a comprehensive understanding of how the layer configuration influences the crystal structure and BIEF direction, and eventually determines the piezoelectric behavior. In this study, the PZT thin films were systematically categorized into four structural types: *α*, *β*, *γ*, and *δ*, each possessing peculiar crystallographic features that account for their respective BIEF directions. Thin films dominated by *β*-PZT, typically accompanied by relatively large compositional gradients and a downward BIEF, tended to exhibit stronger $|e_{31,f}|^-$ responses. By contrast, *γ*-PZT dominant films with suppressed compositional gradients and an upward BIEF resulted in enlarged $|e_{31,f}|^+$. It should also be emphasized that the most enhanced piezoelectric responses in both positive and negative unipolar oscillation were realized in films with average compositions near the MPB. i.e., HL60/45 and HL45/60, respectively. In summary, the diversity in piezoelectric responses highlights the unique advantage of the sol-gel derived epitaxial PZT thin films, particularly their capability for flexible layer configuration design. By tuning the

layer configuration, it becomes possible to optimize the piezoelectric performance for a desired operational mode, whether under positive or negative unipolar oscillation.

CRediT authorship contribution statement

Sang Hyo Kweon: Writing – original draft, Methodology, Investigation, Formal analysis, Data curation. **Kota Kasatani:** Methodology, Investigation, Formal analysis, Data curation. **Isaku Kanno:** Supervision, Funding acquisition, Conceptualization.

Declaration of competing interest

The authors declare that they have no known competing financial interests or personal relationships that could have appeared to influence the work reported in this paper.

Acknowledgements

This research is supported by JST ASPIRE (JPMJAP2312). The authors thank Lichen Bai (State Key Laboratory of Metal Matrix Composites, School of Materials Science and Engineering, Shanghai Jiao Tong University) for assistance with the PFM measurements.

Supplementary materials

Supplementary material associated with this article can be found, in the online version, at doi:10.1016/j.actamat.2026.122162.

References

[1] I. Kanno, Piezoelectric MEMS: ferroelectric thin films for MEMS applications, Jpn. J. Appl. Phys. 57 (2018) 040101.
[2] S. Trolier-McKinstry, P. Muralt, Thin film piezoelectrics for MEMS, J. Electroceram. 12 (2004) 7–17.
[3] J.S. Pulskamp, R.G. Polcawich, R.Q. Rudy, S.S. Bedair, R.M. Proie, T. Ivanov, G. L. Smith, Piezoelectric PZT MEMS technologies for small-scale robotics and RF applications, MRS Bull 37 (2012) 1062–1070.
[4] I. Kanno, Piezoelectric MEMS for energy harvesting, J. Phys.: Conf. Ser. 660 (2015) 012001.
[5] L. Liu, J. Yi, K. Xu, Z. Liu, M. Tang, L. Dai, X. Gao, Y. Liu, S. Wang, Z. Zhang, L. Shu, J.F. Li, S. Zhang, Y. Wang, High piezoelectric property with exceptional stability in self-poled ferroelectric films, Nat. Commun. 15 (2024) 10798.
[6] R. Xu, S.G. Kim, Figures of merits of piezoelectric materials in energy harvesters, PowerMEMS (2012) 464–467.
[7] P.N. Thao, S. Yoshida, S. Tanaka, Fabrication and characterization of PZT fibered-epitaxial thin film on Si for piezoelectric micromachined ultrasound transducer, Micromachines (Basel) 9 (2018) 455.
[8] S. Yoshida, H. Hanzawa, K. Wasa, S. Tanaka, Fabrication and characterization of large figure-of-merit epitaxial PMnN-PZT/Si transducer for piezoelectric MEMS sensors, Sens. Actuators A: Phys. 239 (2016) 201–208.
[9] I. Kanno, H. Kotera, K. Wasa, T. Matsunaga, T. Kamada, R. Takayama, Crystallographic characterization of epitaxial Pb(Zr,Ti)O_3 films with different Zr/Ti ratio grown by radio-frequency-magnetron sputtering, J. Appl. Phys. 93 (2003) 4091–4096.
[10] C.B. Yeager, S. Trolier-McKinstry, Epitaxial Pb(Zr_x,Ti_{1-x})O_3 ($0.30 \leq x \leq 0.63$) films on (100)MgO substrates for energy harvesting applications, J. Appl. Phys. 112 (2012) 074107.
[11] M. Zhu, Z. Du, L. Jing, A.I.Y. Tok, E.H.T. Teo, Optical and electro-optic anisotropy of epitaxial PZT thin films, Appl. Phys. Lett. 107 (2015) 031907.
[12] J. Ouyang, S.Y. Yang, L. Chen, R. Ramesh, A.L. Roytburd, Orientation dependence of the converse piezoelectric constants for epitaxial single domain ferroelectric films, Appl. Phys. Lett. 85 (2004) 278–280.
[13] M. Dekkers, M.D. Nguyen, R. Steenwelle, P.M. te Riele, D.H.A. Blank, G. Rijnders, Ferroelectric properties of epitaxial Pb(Zr,Ti)O_3 thin films on silicon by control of crystal orientation, Appl. Phys. Lett. 95 (2009) 012902.
[14] G. Tan, K. Maruyama, Y. Kanamitsu, S. Nishioka, T. Ozaki, T. Umegaki, H. Hida, I. Kanno, Crystallographic contributions to piezoelectric properties in PZT thin films, Sci. Rep. 9 (2019) 7309.
[15] M.D. Nguyen, M. Dekkers, H.N. Vu, G. Rijnders, Film-thickness and composition dependence of epitaxial thin-film PZT-based mass-sensors, Sens. Actuators A: Phys. 199 (2013) 98–105.
[16] S.H. Kweon, E.J. Kim, G. Tan, I. Kanno, Compositional modification of epitaxial Pb(Zr,Ti)O_3 thin films for high-performance piezoelectric energy harvesters, Adv. Mater. Interfaces (2023) 2300634.
[17] A. Sambri, D. Isarakorn, A. Torres-Pardo, S. Gariglio, P. Janphuang, D. Briand, O. Stèphan, J.W. Reiner, J.M. Triscone, N.F. de Rooij, C.H. Ahn, Epitaxial piezoelectric Pb($Zr_{0.2}Ti_{0.8}$)O_3 thin films on silicon for energy harvesting devices, Smart Mater. Res. (2012) 426048.
[18] H. Funakubo, M. Dekkers, A. Sambri, S. Gariglio, I. Shklyarevskiy, G. Rijnders, Epitaxial PZT films for MEMS printing applications, MRS Bull 37 (2012) 1030–1038.
[19] D. Isarakorn, D. Briand, P. Janphuang, A. Sambri, S. Gariglio, J.-M. Triscone, F. Guy, J.W. Reiner, C.H. Ahn, N.F. de Rooij, The realization and performance of vibration energy harvesting MEMS devices based on an epitaxial piezoelectric thin film, Smart Mater. Struct. 20 (2011) 025015.
[20] G. Kimura, S.H. Kweon, K. Tanaka, Y. Sato, I. Kanno, Internal stress effects on the piezoelectric properties of Pb(Zr,Ti)O_3 superlattice thin films grown on Si substrates, Appl. Phys. Lett. 122 (2023) 122902.
[21] G. Kimura, S.H. Kweon, K. Tanaka, G. Tan, T. Koganezawa, I. Kanno, In situ high-temperature X-ray diffraction measurements of Pb($Zr_{0.58}Ti_{0.42}$)O_3 epitaxial thin films grown on Si substrates, Jpn. J. Appl. Phys. 61 (2022). SN1012.
[22] E.-J. Kim, S.H. Kweon, S. Nahm, Y. Sato, G. Tan, I. Kanno, High output performance of piezoelectric energy harvesters using epitaxial Pb(Zr,Ti)O_3 thin film grown on Si substrate, Appl. Phys. Lett. 121 (2022) 161901.
[23] Y. Sato, G. Kimura, S.H. Kweon, G. Tan, I. Kanno, Disruption of polar order in lead zirconate titanate by composition-modulated artificial superlattice, j. Mater. Sci. 59 (2024) 8134–8146.
[24] D. Akai, M. Yokawa, K. Hirabayashi, K. Matsushita, K. Sawada, M. Ishida, Ferroelectric properties of sol-gel delivered epitaxial Pb(Zr_x,Ti_{1-x})O_3 thin films on Si using epitaxial γ-Al_2O_3 layers, Appl. Phys. Lett. 86 (2005) 202906.
[25] A.A. Talin, S.M. Smith, S. Voight, J. Finder, K. Eisenbeiser, D. Penunuri, Z. Yu, P. Fejes, T. Eschrich, J. Curless, D. Convey, A. Hooper, Epitaxial $PbZr_{.52}Ti_{.48}O_3$ films on $SrTiO_3$/(001)Si substrates deposited by sol–gel method, Appl. Phys. Lett. 81 (2002) 1062–1064.
[26] S. Yin, G. Niu, B. Vilquin, B. Gautier, G. Le Rhun, E. Defay, Y. Robach, Epitaxial growth and electrical measurement of single crystalline Pb($Zr_{0.52}Ti_{0.48}$)O_3 thin film on Si(001) for micro-electromechanical systems, Thin Solid Films 520 (2012) 4572–4575.
[27] G. Tan, S.H. Kweon, I. Kanno, Piezoelectric properties of epitaxial Pb(Zr,Ti)O_3 thin films grown on Si substrates by the sol–gel method, Thin Solid Films 764 (2023) 139612.
[28] S.H. Kweon, Y. Kanayama, G. Tan, T. Koganezawa, I. Kanno, In-situ study on piezoelectric responses of sol-gel derived epitaxial Pb[Zr,Ti]O_3 thin films on Si substrate, J. Eur. Ceram. Soc. 44 (2024) 3887–3894.
[29] H. Li, T. Kijima, H. Yamahara, H. Tabata, M. Seki, Epitaxial single-crystalline PZT thin films on ZrO_2-buffered Si wafers fabricated using spin-coating for mass-produced memristor devices, Adv. Electron. Mater. 11 (2025) 2400280.
[30] F.C. Kartawidjaja, C.H. Sim, J. Wang, Heterolayered PZT thin films of different thicknesses and stacking sequence, J. Mater. Sci. 44 (2009) 5375–5382.
[31] Y. Bastani, N. Bassiri-Gharb, Enhanced dielectric and piezoelectric response in PZT superlattice-like films by leveraging spontaneous Zr/Ti gradient formation, Acta Mater 60 (2012) 1346–1352.
[32] M.D. Nguyen, C.T.Q. Nguyen, T.Q. Trinh, T. Nguyen, T.N. Pham, G. Rijnders, H. N. Vu, Enhancement of ferroelectric and piezoelectric properties in PZT thin films with heterolayered structure, Mater. Chem. Phys. 138 (2013) 862–869.
[33] Z.H. Zhou, J.M. Xue, W.Z. Li, J. Wang, H. Zhu, J.M. Miao, Heterolayered lead zirconate titanate thin films of giant polarization, J. Appl. Phys. 96 (2004) 5706–5711.
[34] D. Zou, S. Liu, C. Zhang, Y. Hong, G. Zhang, Z. Yang, Flexible and translucent PZT films enhanced by the compositionally graded heterostructure for human body monitoring, Nano Energy 85 (2021) 105984.
[35] Y. Tsujiura, S. Kawabe, F. Kurokawa, H. Hida, I. Kanno, Comparison of effective transverse piezoelectric coefficients $e_{31,f}$ of Pb(Zr,Ti)O_3 thin films between direct and converse piezoelectric effects, Jpn. J. Appl. Phys. 54 (2015), 10NA04.
[36] P. Muralt, Texture control and seeded nucleation of nanosize structures of ferroelectric thin films, J. Appl. Phys. 100 (2006) 051605.
[37] Y.L. Tang, Y.L. Zhu, Y.J. Wang, W.Y. Wang, Y.B. Xu, W.J. Ren, Z.D. Zhang, X.L. Ma, Atomic-scale mapping of dipole frustration at 90° charged domain walls in ferroelectric $PbTiO_3$ films, Sci. Rep. 4 (2014) 4115.
[38] F. Calame, P. Muralt, Growth and properties of gradient free sol-gel lead zirconate titanate thin films, Appl. Phys. Lett. 90 (2007) 062907.